Directional effects of antiferromagnetic ordering on the electronic structure in NdSb

Yevhen Kushnirenko[1,2] Brinda Kuthanazhi,[1,2] Lin-Lin Wang,[1] Benjamin Schrunk,[1] Evan O'Leary[1,2] Andrew Eaton[1,2]
Paul C. Canfield,[1,2] and Adam Kaminski[1,2,*]

[1]*Division of Materials Science and Engineering, Ames Laboratory, Ames, Iowa 50011, USA*
[2]*Department of Physics and Astronomy, Iowa State University, Ames, Iowa 50011, USA*

The recent discovery of unconventional surface-state pairs, which give rise to Fermi arcs and spin textures, in antiferromagnetically ordered NdBi raised the interest in rare-earth monopnictides. Several scenarios of antiferromagnetic (AFM) order have been suggested to explain the origin of these states with some of them being consistent with the presence of nontrivial topologies. In this paper, we use angle-resolved photoemission spectroscopy (ARPES) and density-functional-theory (DFT) calculations to investigate the electronic structure of NdSb. We found the presence of distinct domains that have different electronic structures at the surface. These domains correspond to different orientations of magnetic moments in the AFM state with respect to the surface. We demonstrated remarkable agreement between DFT calculations and ARPES that capture all essential changes in the band structure caused by the transition to a magnetically ordered state.

I. INTRODUCTION

Many rare-earth monopnictides order antiferromagnetically at low temperatures due to moment bearing rare-earth ions [1–7]. In the last decade, some materials of this family were predicted to host topological Weyl states [8–10], while in some other materials, topological surface Dirac states are expected to be already present in the paramagnetic (PM) state [11,12] due to band inversion. These predictions are supported by numerous experimental studies [7,13–19]. A recent angle-resolved photoemission spectroscopy (ARPES) study [20] reported the emergence of unconventional surface states (SSs) below the antiferromagnetic (AFM) transition temperature. These new states undergo splitting that leads to the formation of Fermi arcs.

Similarly to other rare-earth monopnictides, NdSb and NdBi have a rocksalt crystal structure and undergo an AFM transition at low temperatures. This transition was observed in neutron diffraction [21–24], magnetization [25–27], resistivity, and specific heat [28] measurements. The transition temperatures reported in these studies for NdSb and NdBi are 15 and 24 K, respectively. In contrast to some other rare-earth monopnictides [29,30], NdSb and NdBi have only one AFM phase with the magnetic structure shown in Fig. 1(a). Two recent ARPES studies [31,32] reported changes in the electronic structure of NdSb upon the AFM transition. However, there was a substantial difference in the band dispersion present below the AFM transition. One study [32] showed the development of two additional features at the Γ point, one of which forms a small round pocket on the Fermi surface (FS). In contrast, another study [31] showed the development of surface-state dispersion at ∼0.2 Å^{-1} away from the Γ point. These surface states form arcs and elliptical pockets of the Fermi surface. Similar surface-state dispersions were also observed in NdBi [20].

Here, we show the existence of different variations of band structures in NdSb below Néel temperature using laser ARPES. These variations coexist in the same sample at different surface locations. Also, we present density-functional-theory (DFT) calculations of the band structure in the AFM ordered NdSb. By comparing the experimental results with DFT calculations, we show that the observed variants of band structures are attributed to domains that have different directions of AFM1 ordering. In addition, we show that magnetically ordered NdBi can have a band structure different from the one reported before. This indicates that NdBi can have different domains as well. The presence of domains with different directions of magnetic ordering was also reported in one more rare-earth monopnictide: CeSb [33]. However, the magnetic ordering in this material is different from the one in NdSb and NdBi, and as a consequence, its electronic structure undergoes different transformations.

II. EXPERIMENTAL DETAILS

Single crystals of NdSb crystals were grown out of Sn flux using an initial concentration of $Nd_4Sb_4Sn_{96}$. The elements were weighed out into a fritted alumina crucible set (Canfield crucible set) [34,35] and sealed in a fused silica tube under partial pressure of argon. The prepared ampules were heated up to 1100 °C over 4 h and held there for 5 h. This was followed by a slow cooling to the decanting temperature of 800 °C over 100 h and decanting of the excess flux using a centrifuge [36]. The cubic crystals obtained were stored and handled in a glove box under nitrogen atmosphere.

Most of the ARPES data were collected using a vacuum ultraviolet (VUV) laser ARPES spectrometer that consists

---

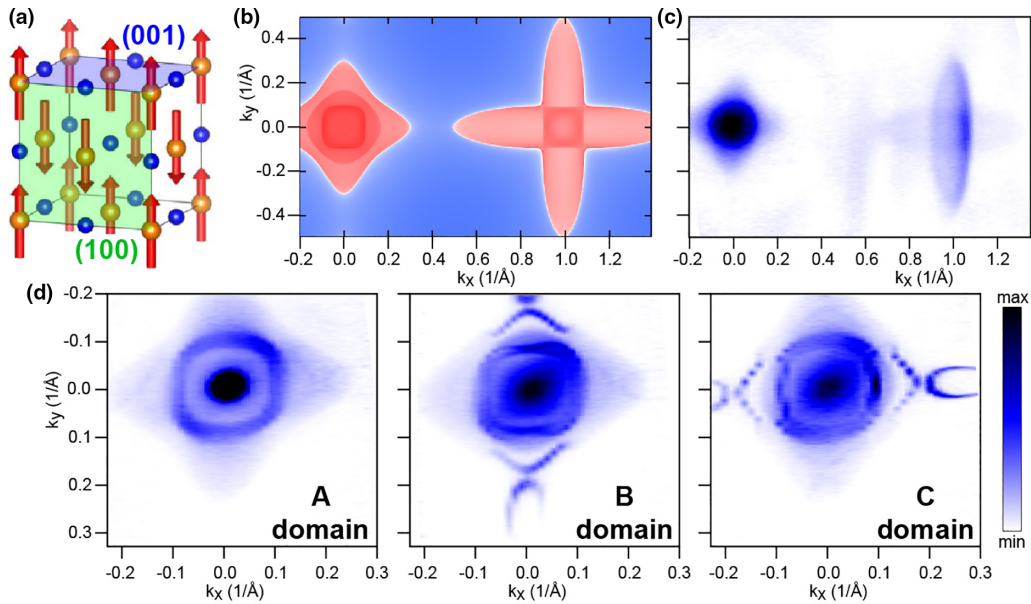*Corresponding author: kaminski@ameslab.gov

FIG. 1. NdSb crystal and band structure. (a) Schematic magnetic structure of AFM1 ordering. Green and blue squares represent (100/010) and (001) planes, respectively. (b) DFT-calculated nonmagnetic Fermi surface. (c) Fermi-surface map measured in the paramagnetic state ($T = 17.5$ K) using a photon energy of 21.2 eV. (d) Three Fermi-surface maps measured at different locations on one sample in the AFM state ($T = 5.5$ K) using a photon energy of 6.7 eV.

of a Scienta DA30 electron analyzer, picosecond Ti:sapphire oscillator, and fourth-harmonic generator [37]. Data from the laser-based ARPES were collected with 6.7 eV photon energy. The angular resolution was set at ~0.1° and 1°, along and perpendicular to the direction of the analyzer slit, respectively, and the energy resolution was set at 2 meV. The VUV laser beam was set to vertical polarization. The diameter of the photon beam on the sample was ~15 μm. Supplementary He-lamp-based ARPES measurements were carried out using an R8000 analyzer and GammaData helium discharge lamp with custom focusing optics. The diameter of the photon beam on the sample was ~1 mm.

III. RESULTS AND DISCUSSION

Figure 1(b) shows a two-dimensional projection of the bulk Fermi surface of paramagnetic NdSb calculated using DFT. As well as other rare-earth monopnictides [6,7,12,17,20,31], it has several hole pockets at the center of the Brillouin zone (BZ) and ellipsoidal electron pockets at its corners. The experimental Fermi-surface (FS) map in Fig. 1(c) was measured in the PM phase using 21.2 eV light from a He lamp. It is in good agreement with DFT calculations. The observed broad FS features are the result of a strong three-dimensionality of the band structure that is projected onto a k_x, k_y plane and limited k_z selectivity of the ARPES experiment.

For further analysis, we measured detailed data sets around the center of the BZ using laser-based ARPES. Figure 1(d) shows three FS maps measured at $T < T_N$ at different locations on the same sample surface cleave. All these maps differ from the map measured in the PM state [Fig. 1(c)] and from each other. As it will be shown later, the first map in Fig. 1(d) corresponds to the case of AFM1 ordering with magnetic moments oriented orthogonal to the sample surface

[001 surface in Fig. 1(a)], while two other maps correspond to the case of AFM1 ordering with magnetic moments oriented parallel to the sample surface [100/010 surface in Fig. 1(a)] along the vertical and horizontal directions.

In Fig. 2, we analyze the effects of magnetic ordering on the electronic band structure at the (001) surface. Parts of the DFT-calculated FS near the Brillouin zone center for AFM1 (001), and PM phases are shown in Figs. 2(a) and 2(b), respectively. In the magnetically ordered state, we observe the suppression of the inner bulk pocket and the appearance of two sharp contours. This suppression is a result of the opening of a hybridization gap (for details, see Appendix B). The inner contour is formed by electronlike surface-state dispersion [see Fig. 2(c)], and the other contour is formed by a folded band and W-shaped surface-state dispersion. To analyze the development of these features and compare them with the calculations, we measured data sets at several temperatures in the magnetically ordered and PM state from the A domain. In Figs. 2(d) and 2(e), we show the temperature evolution of the FS and the band dispersions along a high-symmetry direction. At $T = 6.5$ K, the bottom of the electronlike and the W-shaped dispersion are observed in the experimental data as it is predicted by DFT calculations.

With the temperature increasing, both SS dispersions move to higher binding energies. At the same time, the W-shaped dispersion gradually changes its shape towards a regular parabola. As a result, the FS pockets increase in size. The inner FS pocket appears as a solid circle with a sharp perimeter. This happens because, besides the SS dispersion, which should form just a contour of the FS, there are bulk states above the SS parabola, as is seen from the DFT calculations in Fig. 2(c). In the experimental data, the SS parabola is the most pronounced in the 13.5 K spectrum near the Fermi level. The momentum distribution curve (MDC) obtained from this
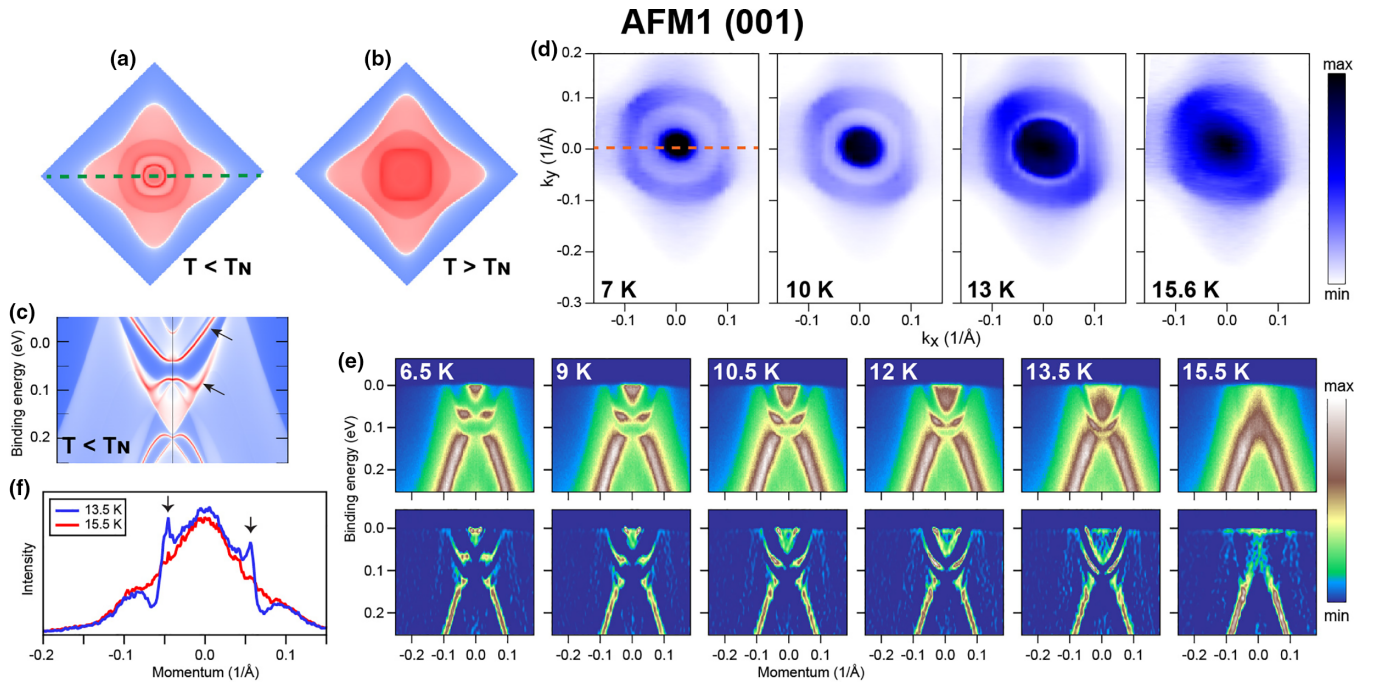
FIG. 2. Band structure at the (001) cleaving plane. (a) and (b) DFT-calculated part of the Fermi surface near the Γ point for AFM and PM phases of NdSb, respectively. (c) DFT-calculated band dispersions along the cut marked with a line in (a). (d) Temperature dependence of the Fermi surface from the A domain. (e) Temperature dependence of band dispersions along the cut marked with a line in (d) and corresponding second derivative plots. (f) E_F MDCs from spectra in (e). All the experimental data in this plot were measured using a photon energy of 6.7 eV. The arrows in (c) mark SS dispersions

spectrum at the Fermi energy (E_F) is shown in Fig. 2(f). Two sharp peaks associated with the surface states can be seen in this curve. Finally, in the paramagnetic state at $T = 15.5$ K, both SS dispersions disappear. Also, from the plots in Fig. 2(e) and MDCs in Fig. 2(f), one can see that in the AFM1 state, a hybridization gap is opening inside the bulk states. These SSs are directly linked to this gap: The electronlike dispersion is the upper boundary of the gap, and the W-shaped dispersion exists inside the gap and partially merges with its lower boundary.

For further analysis, we measured a set of spectra along the Γ-X direction at $T = 10.5$ K using light with different photon energy. These spectra are shown in Fig. 3, together with the corresponding second-derivative plots. This allowed us to access parts of the BZ with different k_z and distinguished SSs from bulk states. Two SS dispersions mentioned above indeed do not shift with photon energy. The only difference between these spectra is the suppression of some parts of them at lower photon energy. This suppression is likely a result of matrix elements. Interestingly, in 6.79 and 6.85 eV spectra, we observe a Dirac-like feature. However, the DFT [Fig. 3(c)] calculations do not predict a Dirac cone there. Two other holelike SS dispersions predicted by DFT calculations can also be observed in the experiment. They correspond to the top of the band located at 300 meV and another one at 420 meV in the experimental data. We can also observe two more relatively sharp dispersions (marked with red arrows in Fig. 3). These dispersions shift with photon energy and are associated with bulk states.

In Fig. 4, we analyze the effects of (100/010) ordering on the surface-state band dispersions. The DFT-calculated FS

and dispersions along the Γ-X and Γ-Y directions are shown in Figs. 4(a)–4(c). These calculations predict the existence of several additional surface states along Γ-X in the magnetically ordered phase, but the most interesting for us are the two outermost surface states, which form Fermi arcs and elliptical electron pockets on the FS. Such states were already observed in the sibling compound NdBi [20]. The calculations successfully reproduce the experimental FS from domains B and C, shown in Fig. 1(d). Both maps demonstrate that the SS Fermi arcs and elliptical pockets are present only along one direction, within a given domain. For further analysis, we plot experimental dispersions along two orthogonal cuts for both maps in Figs. 4(d)–4(g). The cuts along the Γ-X direction show the presence of SSs, namely a pair of K-C split bands near the E_f [Figs. 4(d) and 4(f)], which are responsible for the formation of Fermi arcs and elliptical pockets.

At the same time, we observe no signs of the surface state near the Γ point or suppression of the bulk states in this region similar to those observed in the A-domain data. The SSs are seemingly absent along the Γ-Y direction [Figs. 4(e) and 4(g)]. Taking into account that data sets from all domains were measured under identical experimental conditions (experiment geometry, light polarization, and photon energy), we can conclude that the absence of surface states in the experimental data in one direction is an intrinsic property of this material and not caused by the matrix elements.

The temperature evolution of the spectrum from Fig. 4(d) is shown in Fig. 4(i). The splitting of the SS decreases with increased temperature, and the SS vanishes above T_n. This result agrees with the previous studies of NdSb, and NdBi
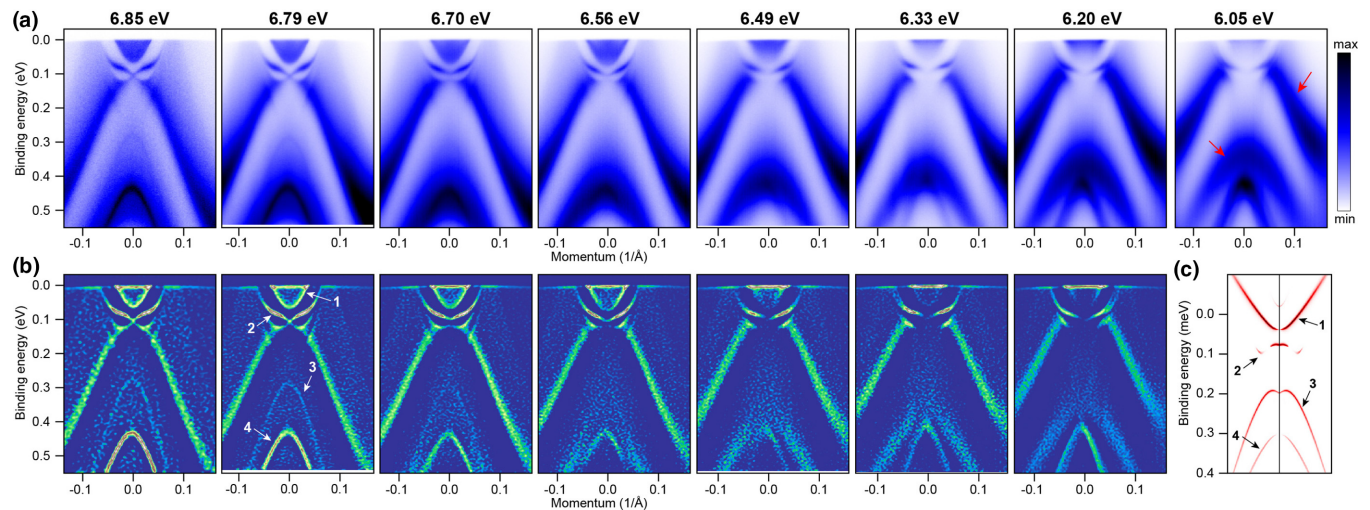
FIG. 3. Photon energy dependence. (a) Spectra measured from the (001) domain along the Γ-X direction using photon energy from 6.05 to 6.85 eV at $T = 10.5$ K. (b) Corresponding plots of second derivatives for the spectra from (a). (c) DFT-calculated surface-state dispersion. The arrows in (b) and (c) mark corresponding SS dispersions. The arrows in (a) mark bulk dispersions.

[20,31]. This behavior is similar to the behavior of the SS on the (001) surface [Fig. 2(e)], where the distance between the surface-state bands also decreases with increasing temperature. Moreover, the absolute positions of the bottoms of these bands are the same for both domain types. Their positions estimated for the (001) surface at $T = 10.5$ K (6.85 eV plot of Fig. 3) are 66 ± 4 and 104 ± 2 meV. Their positions estimated

for the (100) surface at $T = 10.5$ K [Fig. 4(i)] are 68 ± 2 and 105 ± 2 meV. This similarity is not surprising since, in both cases, SSs are formed inside the same hybridization gap. The splitting of the SSs in NdSb is smaller than in NdBi. The distance between the bottom of the electronlike dispersion and the hole-like band at $T = 0.4 T_N$ is 59 meV in NdBi and 46 meV in NdSb.
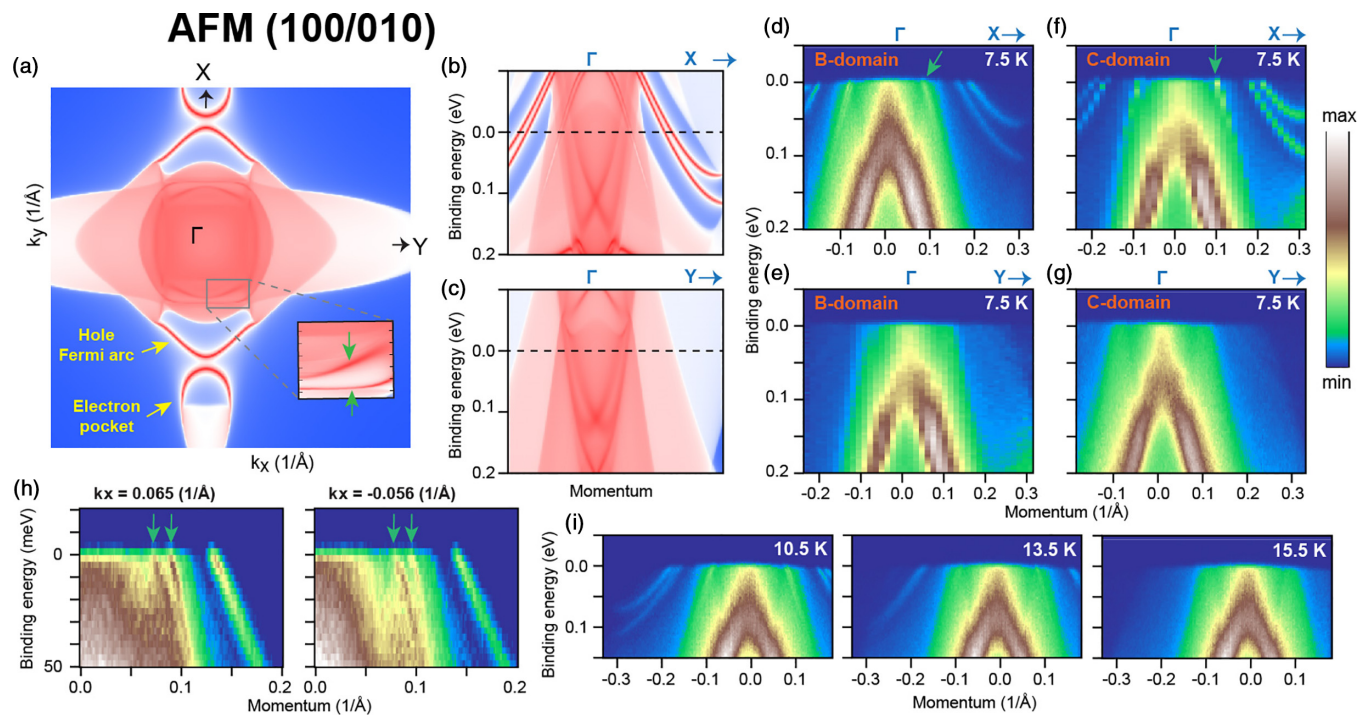

FIG. 4. Band structure in the case of a (100/010) cleavage plane. (a) DFT-calculated Fermi surface for AFM1 state. (b) and (c) DFT-calculated surface state dispersions along Γ-X and Γ-Y in AFM1 state, respectively. (d) and (e) Experimental band structure along the Γ-X and Γ-Y directions obtained from the B-domain data set, respectively. (f) and (g) The same as (d) and (e), respectively, but for the C domain. (h) Cuts parallel to Γ-X taken at $k_x = 0.065$ Å^{-1} and -0.056 Å^{-1}, respectively. (i) Temperature dependence of Γ-X spectrum from (d). The arrows demonstrate the correspondence between particular SS features in the DFT calculations and the experimental data.

TABLE I. The order in which data were collected.

Time (h)	Type	Domain	Temperature (K)	Figure(s)
0.9	FS map	B	5.5	1(d), 4(d), 4(e)
2.6	FS map	A	5.5	1(d), 4(f), 4(g)
4.3	FS map	C	5.5	1(d)
6.4	Spectrum	A	6.5	2(e)
6.5	Spectrum	A	9	2(e)
6.6	Spectrum	A	10.5	2(e)
6.7	Spectrum	A	12	2(e)
6.7	Spectrum	A	13.5	2(e)
6.8	Spectrum	A	15.5	2(e)
7.0	spectrum	B	10.5	4(i)
7.1	Spectrum	B	13.5	4(i)
7.2	Spectrum	B	15.5	4(i)
34.6	FS map	A	13	2(d)
36.4	FS map	A	11	2(d)
37.7	FS map	A	15.6	2(d)
38.5	FS map	A	7	2(d)

In the paramagnetic state at $T \sim 15.5$ K, SS dispersions disappear. The high-temperature spectra in Figs. 2(e) and 4(i) look identical, which indicates that both domain types are indeed formed in the same material. However, after several cycles of heating the sample to $T > T_N$ and cooling it down, we found the same domains at their original locations (for details, see Appendix A). Thus, most likely, the domain type can be predetermined by some factors, e.g., pinned by the strain present in the crystal.

The spectra in Figs. 4(d) and 4(f) exhibit one more SS dispersion (marked with green arrows), which disappears in the paramagnetic state. Under closer inspection, one can see that this dispersion is split into two branches. This can be better seen in the cuts taken slightly off the high-symmetry direction where this splitting is large [see Fig. 4(h)]. As well as the other SS dispersions, this splitting is predicted by DFT calculations. The corresponding features can be found in the calculated FS [Fig. 4(a)].

Elliptical SS pockets and arcs with fourfold symmetry were reported in NdBi in previous ARPES work [20,31]. In analogy to NdSb, these states can be associated with AFM1 (100/010) domains [38]. However, no features associated with (001) domains have been observed in NdBi. In order to prove the presence of (001) domains, we performed more ARPES measurements on NdBi. The results of these measurements are shown in Fig. 5. These spectra do not demonstrate the SS features observed in the previous studies, but they show a hybridization gap at the Γ point and the development of several additional SS dispersions near the Γ point. This makes this band structure similar to the band structure of the (001) domain of NdSb. Also, as well in NdSb, the additional SSs, which are located in the gap, move up with the temperature decreasing. Thus, we can associate this band structure with the AFM(001) ordered domain in NdBi.

IV. CONCLUSIONS

We investigated the evolution of the electron structure in NdSb and NdBi upon an antiferromagnetic transition using ARPES and demonstrated the presence of domains with different configurations of surface states. This result agrees with the earlier neutron diffraction study [23], which also reported the presence of three domain types in NdSb.

The development of a domain with magnetic moments oriented orthogonal to the sample surface causes the formation of a hybridization gap at the Γ point and several additional surface-state dispersions near the Γ point. The development of a domain with magnetic moments oriented parallel to the sample surface causes the formation of a different set of surface states, including an unconventional surface-state pair [20] that forms an arc and an elliptical pocket on the Fermi surface. Except for a Dirac-like feature in the (001) domain which remains unexplained, the observed electron structure of all three domains in NdSb is in exceptional agreement with our DFT calculations for the AFM1 ordered phase.
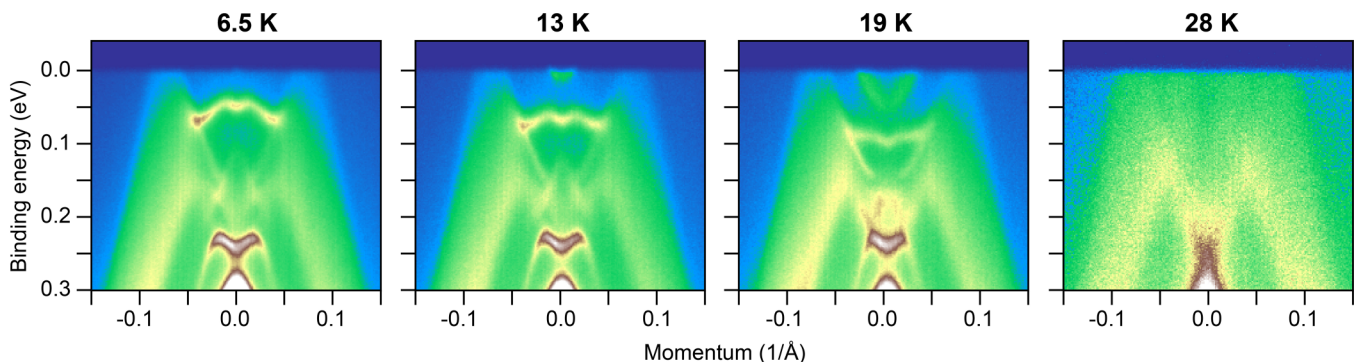
FIG. 5. AFM1 ordering in NdBi [(001) surface]. Temperature dependence of the band structure along the Γ-X direction. $T_N = 24$ K.
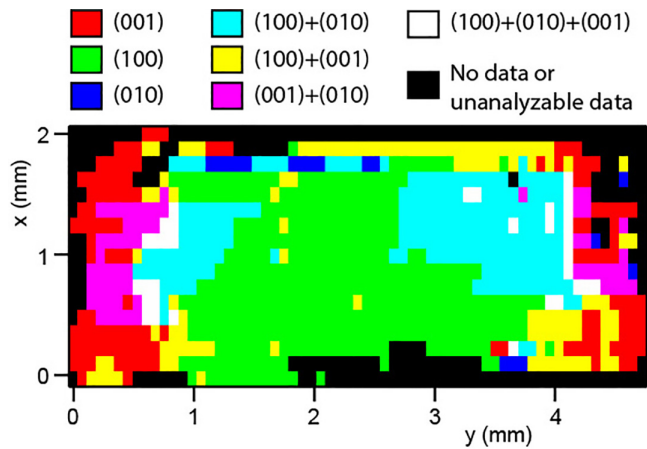
FIG. 6. NdSb: additional data. Domain map measured using ARPES. Red, green, and blue colors represent parts of the sample where there is one domain type. Cyan, magenta, yellow, and white colors represent parts of the sample where we observed the superposition of signals from several domains.

APPENDIX A: REPRODUCIBILITY

Most of the data presented in the main text were collected from one sample. The order in which data were collected is shown in Table I. We see that after heating the sample up and cooling it down, the band structure measured from the part of the sample where the B domain was, did not change. Moreover, the band structure measured from the part of the sample where the A domain was, did not change after three cycles of temperature variation. Also, it shows that under the experimental conditions, the aging of the sample surface is negligible: The map measured from the A domain soon after cleaving the sample [Fig. 1(d)] looks identical to a similar map measured 24 h later [Fig. 2(d)].

The mapping of another sample (Fig. 6) has shown that it also has parts where each one of the three domain types is dominant, as well as parts where we observe the superposition of signals from several domains. To obtain this map, we scanned the raster by moving the sample when the laser beam position was static. The experiment was performed at $T = 10.5$ K using 6.7 eV light. To access different BZ parts the experiment was repeated for five different sample tilt angles ($-17°$, $-5°$, $0°$, $5°$, and $17°$). These data sets were analyzed for features specific to a particular domain type.

APPENDIX B: DFT CALCULATIONS

The density-functional-theory (DFT)-calculated surface spectral function of NdSb AFM $1q$ on (001) and (100)/(010) surfaces are shown in Fig. 7. All DFT [39,40] calculations with spin-orbit coupling (SOC) were performed with the Perdew-Burke-Ernzerhof (PBE) [41] exchange-correlation
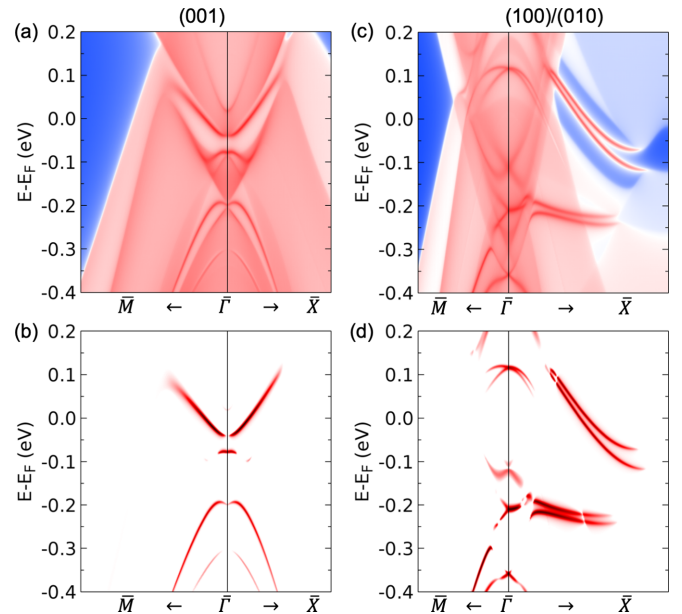

FIG. 7. DFT-calculated surface spectral function of NdSb AFM $1q$ on (a) (001) and (c) (100)/(010) surfaces. The corresponding surface only contributions are plotted in (b) and (d), respectively, to highlight the surface bands. Notably on (001), the hybridization gap and the associated surface states around the Γ point as discussed in Fig. 2 has an overall bulk band projection background, in contrast to the unconventional surface-state pairs away from the Γ point on (100)/(010) residing in the hybridization gap without such a background.

functional using a plane-wave basis set and projector augmented-wave method [42], as implemented in the Vienna *ab initio* simulation package (VASP) [43,44]. Using maximally localized Wannier functions [45,46], tight-binding models were constructed to reproduce closely the band structure including SOC within $E_F \pm 1$ eV with Nd s-d-f and Sb p orbitals. The surface spectral function and 2D Fermi surface (FS) were calculated with the surface Green's function methods [47,48] as implemented in WANNIERTOOLS [49]. In the DFT calculations, we used a kinetic energy cutoff of 254 eV, a Gaussian smearing of 0.05 eV, a Γ-centered Monkhorst-Pack [50] ($11 \times 11 \times 8$) k-point mesh for the $1q$ tetragonal unit cell and an ($8 \times 8 \times 8$) k-point mesh for the $2q$ cubic unit cell. For band-structure calculations, we have used the experimental lattice parameters of 6.336 Å. To account for the strongly localized Nd $4f$ orbitals in NdSb, an on-site Hubbard-like [51] $U = 6.3$ eV and $J = 0.7$ eV have been used. Our DFT+U+SOC calculation on NdSb $1q$ and $2q$ gives a similar spin moment of $2.7\mu_B$ and an orbital moment of $5.7\mu_B$ in the opposite direction, resulting in a total magnetic moment of $3.0\mu_B$ on Nd.

[1] N. Nereson and G. Arnold, J. Appl. Phys. **42**, 1625 (1971).

[2] H. Bartholin, P. Burlet, S. Quezel, J. Rossat-Mignod, and O. Vogt, J. Phys. Colloq. **40**, C5 (1979).

[3] P. C. Canfield and Z. Fisk, Philos. Mag. B **65**, 1117 (1992).

[4] H. Kumigashira, S.-H. Yang, T. Yokoya, A. Chainani, T. Takahashi, A. Uesawa, T. Suzuki, O. Sakai, and Y. Kaneta, Phys. Rev. B **54**, 9341 (1996).

[5] P. C. Canfield and I. R. Fisher, J. Cryst. Growth **225**, 155 (2001).

[6] Y. Wu, Y. Lee, T. Kong, D.-x. Mou, R. Jiang, L. Huang, S. L. Bud'ko, P. C. Canfield, and A. Kaminski, Phys. Rev. B **96**, 035134 (2017).

[7] K. Kuroda, M. Ochi, H. S. Suzuki, M. Hirayama, M. Nakayama, R. Noguchi, C. Bareille, S. Akebi, S. Kunisada, T. Muro, M. D. Watson, H. Kitazawa, Y. Haga, T. K. Kim, M. Hoesch, S. Shin, R. Arita, and T. Kondo, Phys. Rev. Lett. **120**, 086402 (2018).

[8] C. Guo, C. Cao, M. Smidman, F. Wu, Y. Zhang, F. Steglich, F.-C. Zhang, and H. Yuan, npj Quantum Mater. **2**, 39 (2017).

[9] Z. Li, D.-D. Xu, S.-Y. Ning, H. Su, T. Iitaka, T. Tohyama, and J.-X. Zhang, Int. J. Mod. Phys. B **31**, 1750217 (2017).

[10] Z. Huang, C. Lane, C. Cao, G.-X. Zhi, Y. Liu, C. E. Matt, B. Kuthanazhi, P. C. Canfield, D. Yarotski, A. J. Taylor, and J.-X. Zhu, Phys. Rev. B **102**, 235167 (2020).

[11] M. Zeng, C. Fang, G. Chang, Y.-A. Chen, T. Hsieh, A. Bansil, H. Lin, and L. Fu, arXiv:1504.03492.

[12] X. Duan, F. Wu, J. Chen, P. Zhang, Y. Liu, H. Yuan, and C. Cao, Commun. Phys. **1**, 71 (2018).

[13] Y. Wu, T. Kong, L.-L. Wang, D. D. Johnson, D. Mou, L. Huang, B. Schrunk, S. L. Bud'ko, P. C. Canfield, and A. Kaminski, Phys. Rev. B **94**, 081108(R) (2016).

[14] X. H. Niu, D. F. Xu, Y. H. Bai, Q. Song, X. P. Shen, B. P. Xie, Z. Sun, Y. B. Huang, D. C. Peets, and D. L. Feng, Phys. Rev. B **94**, 165163 (2016).

[15] J. Nayak, S.-C. Wu, N. Kumar, C. Shekhar, S. Singh, J. Fink, E. E. Rienks, G. H. Fecher, S. S. Parkin, B. Yan *et al.*, Nat. Commun. **8**, 13942 (2017).

[16] R. Lou, B.-B. Fu, Q. N. Xu, P.-J. Guo, L.-Y. Kong, L.-K. Zeng, J.-Z. Ma, P. Richard, C. Fang, Y.-B. Huang, S.-S. Sun, Q. Wang, L. Wang, Y.-G. Shi, H. C. Lei, K. Liu, H. M. Weng, T. Qian, H. Ding, and S.-C. Wang, Phys. Rev. B **95**, 115140 (2017).

[17] H. Oinuma, S. Souma, K. Nakayama, K. Horiba, H. Kumigashira, M. Yoshida, A. Ochiai, T. Takahashi, and T. Sato, Phys. Rev. B **100**, 125122 (2019).

[18] A. P. Sakhya, S. Kumar, A. Pramanik, R. P. Pandeya, R. Verma, B. Singh, S. Datta, S. Sasmal, R. Mondal, E. F. Schwier *et al.*, Phys. Rev. B **106**, 085132 (2022).

[19] C. E. Matt, Y. Liu, H. Pirie, N. C. Drucker, N. H. Jo, B. Kuthanazhi, Z. Huang, C. Lane, J.-X. Zhu, P. C. Canfield, and J. E. Hoffman, Phys. Rev. B **105**, 085134 (2022).

[20] B. Schrunk, Y. Kushnirenko, B. Kuthanazhi, J. Ahn, L.-L. Wang, E. O'Leary, K. Lee, A. Eaton, A. Fedorov, R. Lou, V. Voroshnin, O. J. Clark, J. Sánchez-Barriga, S. L. Bud'ko, R.-J. Slager, P. C. Canfield, and A. Kaminski, Nature (London) **603**, 610 (2022).

[21] N. Nereson and V. Struebing, in *Magnetism and Magnetic Materials - 1971 (Seventeenth Annual Conference)*, edited by C. D. Graham, Jr. and J. J. Rhyne, AIP Conf. Proc. No. 5 (American Institute of Physics, New York, 1972), pp. 1385–1389.

[22] P. Schobinger-Papamantellos, P. Fischer, O. Vogt, and E. Kaldis, J. Phys. C: Solid State Phys. **6**, 725 (1973).

[23] D. Mukamel, J. M. Hastings, L. M. Corliss, and J. Zhuang, Phys. Rev. B **32**, 7367 (1985).

[24] P. Manfrinetti, A. Provino, A. Morozkin, and O. Isnard, J. Alloys Compd. **487**, L28 (2009).

[25] P. Bak and P.-A. Lindgard, J. Phys. C: Solid State Phys. **6**, 3774 (1973).

[26] Y. Zhou, X. Zhu, S. Huang, X. Chen, Y. Zhou, C. An, B. Zhang, Y. Yuan, Z. Xia, C. Gu *et al.*, Phys. Rev. B **96**, 205122 (2017).

[27] Y. Wang, J. H. Yu, Y. Q. Wang, C. Y. Xi, L. S. Ling, S. L. Zhang, J. R. Wang, Y. M. Xiong, T. Han, H. Han, J. Yang, J. Gong, L. Luo, W. Tong, L. Zhang, Z. Qu, Y. Y. Han, W. K. Zhu, L. Pi, X. G. Wan, C. Zhang, and Y. Zhang, Phys. Rev. B **97**, 115133 (2018).

[28] N. Wakeham, E. D. Bauer, M. Neupane, and F. Ronning, Phys. Rev. B **93**, 205152 (2016).

[29] J. Rossat-Mignod, P. Burlet, J. Villain, H. Bartholin, W. Tcheng-Si, D. Florence, and O. Vogt, Phys. Rev. B **16**, 440 (1977).

[30] B. Kuthanazhi, N. H. Jo, L. Xiang, S. L. Bud'ko, and P. C. Canfield, Philos. Mag. **102**, 542 (2022).

[31] Y. Kushnirenko, B. Schrunk, B. Kuthanazhi, L.-L. Wang, J. Ahn, E. O'Leary, A. Eaton, S. L. Bud'ko, R.-J. Slager, P. C. Canfield, and A. Kaminski, Phys. Rev. B **106**, 115112 (2022).

[32] A. P. Sakhya, B. Wang, F. Kabir, C.-Y. Huang, M. M. Hosen, B. Singh, S. Regmi, G. Dhakal, K. Dimitri, M. Sprague, R. Smith, E. D. Bauer, F. Ronning, A. Bansil, and M. Neupane, Phys. Rev. B **106**, 235119 (2022).

[33] K. Kuroda, Y. Arai, N. Rezaei, S. Kunisada, S. Sakuragi, M. Alaei, Y. Kinoshita, C. Bareille, R. Noguchi, M. Nakayama, S. Akebi, M. Sakano, K. Kawaguchi, M. Arita, S. Ideta, K. Tanaka, H. Kitazawa, K. Okazaki, M. Tokunaga, Y. Haga *et al.*, Nat. Commun. **11**, 2888 (2020).

[34] P. C. Canfield, T. Kong, U. S. Kaluarachchi, and N. H. Jo, Philos. Mag. **96**, 84 (2016).

[35] Canfield Cruible Sets, https://lspceramics.com/canfield-crucible-sets-2/.

[36] P. C. Canfield, Rep. Prog. Phys. **83**, 016501 (2020).

[37] R. Jiang III, D. Mou, Y. Wu, L. Huang, C. D. McMillen, J. Kolis, H. G. Giesber, J. J. Egan, and A. Kaminski, Rev. Sci. Instrum. **85**, 033902 (2014).

[38] L.-L. Wang, J. Ahn, R.-J. Slager, Y. Kushnirenko, B. G. Ueland, A. Sapkota, B. Schrunk, B. Kuthanazhi, R. J. McQueeney, P. C. Canfield *et al.*, Commun. Phys. **6**, 78 (2023).

[39] P. Hohenberg and W. Kohn, Phys. Rev. **136**, B864 (1964).

[40] W. Kohn and L. J. Sham, Phys. Rev. **140**, A1133 (1965).

[41] J. P. Perdew, K. Burke, and M. Ernzerhof, Phys. Rev. Lett. **77**, 3865 (1996).

[42] P. E. Blöchl, Phys. Rev. B **50**, 17953 (1994).

[43] G. Kresse and J. Furthmüller, Phys. Rev. B **54**, 11169 (1996).

[44] G. Kresse and J. Furthmüller, Comput. Mater. Sci. **6**, 15 (1996).

[45] N. Marzari and D. Vanderbilt, Phys. Rev. B **56**, 12847 (1997).

[46] I. Souza, N. Marzari, and D. Vanderbilt, Phys. Rev. B **65**, 035109 (2001).

[47] M. P. L. Sancho, J. M. L. Sancho, and J. Rubio, J. Phys. F: Met. Phys. **14**, 1205 (1984).

[48] M. P. L. Sancho, J. M. L. Sancho, J. M. L. Sancho, and J. Rubio, J. Phys. F: Met. Phys. **15**, 851 (1985).

[49] Q. Wu, S. Zhang, H.-F. Song, M. Troyer, and A. A. Soluyanov, Comput. Phys. Commun. **224**, 405 (2018).

[50] H. J. Monkhorst and J. D. Pack, Phys. Rev. B **13**, 5188 (1976).

[51] A. I. Liechtenstein, V. I. Anisimov, and J. Zaanen, Phys. Rev. B **52**, R5467(R) (1995).